

1. INTRODUCTION

The Large Area Telescope (LAT) went into orbit on 2008 June 11 aboard the Fermi Gamma-ray Space Telescope (formerly GLAST; [Atwood et al. 2009](#)). Gamma-ray pulsations from the pulsar PSR J2021+3651 ([Roberts et al. 2002](#)) were detected during the first weeks of commissioning. The LAT was built to ad-

dress, along with other pressing questions in high-energy astrophysics, the extent to which gamma-ray emission by pulsars is a rule, and thereby to better understand the mechanisms by which the kinetic energy of a rotating neutron star is transformed into intense beams of radiation. The discovery of a pulsed gamma-ray signal from PSR J2021+3651 was reported using AGILE, the "Astrorivelatore Gamma a Immagini Leggiero", by [Halpern et al. \(2008\)](#).

Following the detection of at least six high-energy gamma-ray pulsars by the Energetic Gamma Ray Experiment Telescope (EGRET) on the Compton Gamma Ray Observatory (see summary by [Thompson 2004](#)), observers sought positional coincidences of newly-discovered pulsars (e.g., [Kramer et al. 2003](#)) with EGRET catalog sources ([Hartman et al. 1999](#)) or searched the EGRET error boxes for new radio pulsars (e.g., [Crawford et al. 2006](#)).

In one such search, [Roberts et al. \(2002\)](#) discovered PSR J2021+3651 with period 103.7 ms within the GeV error box associated with 3EG J2021+3716 ([Lamb & McComb 1997](#); [Roberts et al. 2001](#)). PSR J2021+3651 is young (characteristic timing age 17 kyr) and energetic ($\dot{E} = 3.38 \times 10^{36}$ ergs s⁻¹). The NE2001 model ([Cordes & Lazio 2002](#)) for the Galactic distribution of free electrons for this line of sight ($l = 75.21^\circ$; $b = 0.13^\circ$) and the dispersion measure of DM = 370 pc cm⁻³ suggest a distance of $D = 12$ kpc, with a fractional uncertainty that can exceed 50%. Subsequent investigations with the Chandra X-ray Observatory revealed a pulsar wind nebula (PW N) and possible pulsations in X-rays ([Hessels et al. 2004](#)). The torus of this "Dragon" PW N is clearly resolved, providing an estimate of the orientation of the pulsar's spin axis relative to the observer's line of sight of 85.1° ([Van Etten et al. 2008](#)). All authors point out that such a large distance implies high efficiency for the conversion of spin-down power into gamma-rays, becoming unphysical ($> 100\%$) for some beam scenarios, and explore different ways to constrain the distance. The X-ray spectra are consistent with a distance of 2 to 4 kpc. This paper adds new elements to the discussion: a more

¹⁰ Dipartimento di Fisica "G. Galilei", Università di Padova, I-35131 Padova, Italy

¹¹ Department of Physics, Royal Institute of Technology (KTH), AlbaNova, SE-106 91 Stockholm, Sweden

¹² Department of Physics, Center for Cosmology and Astrophysics, The Ohio State University, Columbus, OH 43210

¹³ Laboratoire Leprince-Ringuet, Ecole polytechnique, CNRS/IN2P3, Palaiseau, France

¹⁴ Dipartimento di Fisica "M. Merlin" dell'Università e del Politecnico di Bari, I-70126 Bari, Italy

¹⁵ Istituto Nazionale di Fisica Nucleare, Sezione di Bari, 70126 Bari, Italy

¹⁶ Department of Physics, University of Washington, Seattle, WA 98195-1560

¹⁷ Columbia Astrophysics Laboratory, Columbia University, New York, NY 10027

¹⁸ INFN-Istituto di Astrofisica Spaziale e Fisica Cosmica, I-20133 Milano, Italy

¹⁹ Istituto Nazionale di Fisica Nucleare, Sezione di Perugia, I-06123 Perugia, Italy

²⁰ Dipartimento di Fisica, Università degli Studi di Perugia, I-06123 Perugia, Italy

²¹ George Mason University, Fairfax, VA 22030

²² NASA Goddard Space Flight Center, Greenbelt, MD 20771

²³ Laboratoire de Physique et Chimie de l'Environnement, LPCE UMR 6115 CNRS, F-45071 Orleans Cedex 02, and Station de radioastronomie de Nancy, Observatoire de Paris, CNRS/INSU, F-18330 Nancy, France

²⁴ Laboratoire de Physique Théorique et Astroparticules, Université Montpellier 2, CNRS/IN2P3, Montpellier, France

²⁵ Department of Physics and Astronomy, Sonoma State University, Rohnert Park, CA 94928-3609

²⁶ Department of Physics, Stockholm University, AlbaNova, SE-106 91 Stockholm, Sweden

²⁷ Agenzia Spaziale Italiana (ASI) Science Data Center, I-00044 Frascati (Roma), Italy

²⁸ National Radio Astronomy Observatory (NRAO), Charlottesville, VA 22903

²⁹ Dipartimento di Fisica, Università di Udine and Istituto Nazionale di Fisica Nucleare, Sezione di Trieste, Gruppo Collegato di Udine, I-33100 Udine, Italy

³⁰ Istituto Universitario di Studi Superiori (IUSS), I-27100 Pavia, Italy

³¹ CNRS/IN2P3, Centre d'Études Nucleaires Bordeaux Gradignan, UMR 5797, Gradignan, 33175, France

³² Université de Bordeaux, Centre d'Études Nucleaires Bordeaux Gradignan, UMR 5797, Gradignan, 33175, France

³³ Jodrell Bank Centre for Astrophysics, School of Physics and Astronomy, University of Manchester, M13 9PL, UK

³⁴ Arecibo Observatory, Arecibo, Puerto Rico 00612

³⁵ Department of Physical Science and Hiroshima Astrophysical Science Center, Hiroshima University, Higashi-Hiroshima 739-8526, Japan

³⁶ University of Maryland, College Park, MD 20742

³⁷ Corresponding authors: D. A. Smith, smith@cenbg.in2p3.fr; M. Kerr, kerr@uwashington.edu; L. Guillemot, guillemot@cenbg.in2p3.fr.

³⁸ Australia Telescope National Facility, CSIRO, Epping NSW 1710, Australia

³⁹ Department of Physics, Tokyo Institute of Technology, Meguro City, Tokyo 152-8551, Japan

⁴⁰ Cosmic Radiation Laboratory, Institute of Physical and Chemical Research (RIKEN), Wako, Saitama 351-0198, Japan

⁴¹ UCO/Lick Observatories, Santa Cruz, CA 95064

⁴² Centre d'Étude Spatiale des Rayonnements, CNRS/UPS, BP 44346, F-30128 Toulouse Cedex 4, France

⁴³ Department of Physics, West Virginia University, Morgantown, WV 26506

town, WV 26506

⁴⁴ Center for Research and Exploration in Space Science and Technology (CRESTT), NASA Goddard Space Flight Center, Greenbelt, MD 20771

⁴⁵ Istituto Nazionale di Fisica Nucleare, Sezione di Roma "Tor Vergata", I-00133 Roma, Italy

⁴⁶ Max-Planck Institut für extraterrestrische Physik, 85748 Garching, Germany

⁴⁷ Department of Physics and Astronomy, University of Denver, Denver, CO 80208

⁴⁸ Institute of Space and Astronautical Science, JAXA, 3-1-1 Yoshinodai, Sagamihara, Kanagawa 229-8510, Japan

⁴⁹ Institut de Ciències de l'Espai (IEEC-CSIC), Campus UAB, 08193 Barcelona, Spain

⁵⁰ NYCB Real-Time Computing Inc., Lattingtown, NY 11560-1025

⁵¹ Department of Chemistry and Physics, Purdue University Calumet, Hammond, IN 46323-2094

⁵² Institució Catalana de Recerca i Estudis Avançats (ICREA), Barcelona, Spain

⁵³ Consorzio Interuniversitario per la Fisica Spaziale (CIFS), I-10133 Torino, Italy

⁵⁴ Dipartimento di Fisica, Università di Roma "Tor Vergata", I-00133 Roma, Italy

⁵⁵ School of Pure and Applied Natural Sciences, University of Kalmar, SE-391 82 Kalmar, Sweden

detailed gamma-ray light curve with phase-resolved spectroscopy, a detailed comparison of the gamma-ray light curve with the predictions of various models, and radio polarization measurements.

PSR J2021+ 3651 illustrates the importance of sustained monitoring of pulsar timing. It is one of the more than 200 pulsars with $E > 10^{34}$ ergs s^{-1} monitored by the program coordinated between the radio and X-ray timing community and the Fermi LAT team (Smith et al. 2008). PSR J2021+ 3651, like many young pulsars, exhibits timing noise. Not only do contemporaneous timing allow accurate comparisons between radio and gamma-ray light curves, but folding at a known period provides significantly greater sensitivity than searching for a periodicity. McLaughlin & Cordes (2004) detected significant periodicities for PSR J2021+ 3651 in two of eight EGRET viewing periods (VPs) containing the pulsar by extrapolating the timing solution and searching around a range of period and period derivative. The light curve was consistent between the two VPs and is similar to the LAT light curve. However, they were unable to detect significant pulsations in the other six VPs. PSR J2021+ 3651 was one of only two pulsars detected by them in this manner due to the large number of trials needed when extrapolating timing solutions back several years. The ongoing pulsar monitoring for Fermi greatly reduces such problems.

2. OBSERVATIONS

The LAT is a pair-production telescope. It consists of tungsten foil and silicon microstrip converter/trackers (pair conversion and track measurement); hodoscopic cesium iodide calorimeters (energy measurement); plastic scintillator anticoincidence detectors (charged particle rejection); and a programmable trigger and data acquisition system. The LAT's excellent sensitivity stems from a large effective area (~ 8000 cm²) and superior angular resolution. The broad field of view (2.4 steradian) allows long exposures to the whole sky. The LAT is sensitive to gamma-rays with energy > 20 MeV. Verification of the on-orbit response is continuing but appears consistent with expectations⁵⁶.

Gamma-ray events recorded with the LAT have timestamps that derive from a GPS clock on the Fermi satellite. Ground tests using cosmic ray muons demonstrated that the LAT measures event times with a precision significantly better than 1 μ s. On orbit, satellite telemetry indicates comparable accuracy. Transformation to the solar system barycenter and phase calculations were done with the Fermi LAT "Science Tools", shown to be accurate to better than a few μ s for isolated pulsars (Smith et al. 2008). Degradation of the barycentered time resolution from uncertainty in Fermi's position is negligible. End-to-end performance of the timing systems was confirmed using the bright EGRET pulsars. The LAT gamma-ray phases of these pulsars relative to the radio phases agree with previous measurements (e.g., Fierro et al. 1998).

Data were acquired in two different Fermi observing modes. Between 2008 June 30 and August 3 the LAT was often pointed near the northern orbital pole ($l = 18h40m$, $b = 60$, or $l = 90$; $b = 25$, in mid-July).

Since then, Fermi has been scanning the entire sky every two orbits (approximately 3 hours). The data used here were acquired through 2008 November 15. The "diuse" event selection was used ("Pass 6", version 1, see Atwood et al. 2009), leaving a background due to charged cosmic rays comparable to or less than the extragalactic diffuse gamma-ray emission. Gamma-rays with measured zenith angles greater than 105° were excluded, due to the intense gamma-ray emission from the Earth's limb caused by cosmic rays interacting in the atmosphere.

PSR J2021+ 3651 is being observed by the timing consortium supporting Fermi observations with the NRAO Green Bank Telescope (GBT), the NAIC Arecibo telescope, and the Lovell telescope at Jodrell Bank. The combined usage of these observatories provides simultaneously good timing precision and good sampling. The most precise timing measurements are acquired at Arecibo and GBT, while the best sampling is obtained with GBT and Jodrell Bank; the observational setup at the latter is described in Hobbs et al. (2004). The WAPP spectrometer used at Arecibo is described in Dowd et al. (2000). Here we use a rotational ephemeris based on GBT data.

The phase-connected ephemeris for PSR J2021+ 3651 listed in Table 1, contemporaneous with the Fermi observations, was derived from 21 observations obtained between 2008 June 17 and November 15⁵⁷. The DE405 solar system ephemeris was used (Standish 1998). The pulsar was observed at a center frequency of either 1950 MHz or 1550 MHz with the GBT Pulsar Spigot (Krajan et al. 2005), yielding total power samples every 81.92 μ s in each of 768 frequency channels over a bandwidth of 600 MHz. Each observation lasted for 5 minutes, from which we derived a time of arrival with typical uncertainty of 0.2 ms. PSR J2021+ 3651 exhibits rotational instability that is significant over the span of 5 months. We used the TEMPO timing software⁵⁸ and describe the pulsar rotation well by fitting for its frequency and first two derivatives. This timing solution had small unmodeled residual features ($\chi^2 = 1.4$), with a post-timing χ^2 of 0.2 ms. The DM is used to correct the time of arrival of the radio pulse to in-site frequency for absolute phase comparison with the gamma-ray profile. Because the radio profiles of PSR J2021+ 3651 are significantly scattered at the frequencies that we use for timing, an ordinary TEMPO fit biases the DM upwards from its true value. In order to correct for this, we fit scattering models to the (assumed intrinsic) profile at 5 GHz until the resulting profiles matched the observed ones. The measured pulse broadening (scaled to 1 GHz) appears to be about a factor of two larger than previously estimated by Hessels et al. (2004). The corresponding $DM = 367.5 \pm 1$ pc cm⁻³ is 0.5% smaller than the value without this correction, where the estimated uncertainty is dominated by systematic effects. The resulting phase uncertainty after extrapolation from 1.95 GHz to in-site frequency is 0.01.

In addition to the Spigot observations, we observed the pulsar at 2000 MHz using the new Green Bank UL-

⁵⁷ This and other ephemerides used in Fermi results will be available from the Fermi Science Support Center (FSSC) data servers at <http://fermi.gsfc.nasa.gov/ssc>.

⁵⁸ <http://www.atnf.csiro.au/research/pulsar/tempo/>

⁵⁶ http://www-glast.slac.stanford.edu/software/IS/glast_lat_performance.htm.

time Pulsar Processing Instrument (GUPPI)⁵⁹ at the GBT for 1.3 hours. GUPPI provides full-polarization spectra in 2048 channels over 800 MHz of bandwidth every 40.96 s. The resulting data were polarization- and flux-calibrated based on observations of a local pulsed noise signal and the bright quasar J1445+0958. Analysis was performed using the P SRCHIVE software package (Hotan et al. 2004).

We re-analyzed the 20.8 ks Chandra ACIS-S continuous clocking data from MJD 52682 described in Hessels et al. (2004), using the current version of Chandra analysis software, and a timing solution built from near-contemporaneous radio observations acquired with the Lovell telescope at Jodrell Bank. The light curve is shown in Figure 1. The deviation from a flat light curve is slightly more significant (4.5%) than that reported by Hessels et al. (3.7%), has the same overall shape as their Figure 3, but is shifted in phase. The first peak seems to be within 0.1 in phase with the first gamma-ray peak albeit with weak statistics. Hessels et al. discuss the possibility of a non-thermal component from the X-ray point source, and Van Etten et al. measure this component's flux: the ratio of the X-ray non-thermal flux to the gamma-ray flux is 10^4 , greater than that observed for Vela (10^3) or for Geminga (10^2 , Bignami & Caraveo 1996). The X-ray light curve also resembles those of other established gamma-ray pulsars (Kaspi et al. 2006).

3. RESULTS

The LAT orientation with respect to the celestial sphere has been calibrated to a precision of $30''$, using more than a dozen known bright point sources. The Chandra-derived position of PSR J2021+3651 is $0.62''$ from the center of the gamma-ray 68% containment contour, which has a $0.75''$ radius. Figure 2 shows the distribution of counts for the region surrounding the pulsar.

3.1. Light curve

The top frame of Figure 1 shows the phase histogram for the gamma-ray events with energies > 100 MeV, within an energy-dependent 68% angular containment radius of the radio pulsar position. There are two peaks: the first peak (P1) is the phase interval $0.13 < \phi < 0.20$, and P2 is $0.58 < \phi < 0.68$. Both peaks are well-fit by a Lorentzian function, yielding full widths at half-maximum of 0.021 ± 0.002 and 0.053 ± 0.006 rotations, respectively, separated by $\Delta\phi = 0.468 \pm 0.002$. P1 lags the maximum of the 2 GHz radio peak shown in the bottom frame by $\Delta t_{\text{radio}} = 0.162 \pm 0.004 \pm 0.01$ rotations of the neutron star. The first uncertainty is statistical, the second is due to the uncertainty in the DM. The intermediate frames show three energy bands: 100 MeV to 1 GeV; 1–3 GeV; and > 3 GeV. P1 fades with increasing energy, whereas P2 persists. The highest energy photon in this sample has 12 GeV, in P2. The peak positions are stable with energy to within 0.01 in phase.

3.2. Spectrum

The spectral shape, the cutoff energy, and the integral energy flux are observables that can be compared with pulsar emission models. PSR J2021+3651 is located in the Cygnus region where diffuse emission is

bright and there are poorly resolved neighboring sources (Fig. 2). Whole-mast spectra in the 3rd EGRET catalog were well-modeled by a single power-law spectrum, 3EG J2021+3716 was a clear exception. A two-power-law fit, with the break point fixed at 1 GeV, gave a reduced $\chi^2 = 0.55$, compared to reduced $\chi^2 = 2.8$ for the simple power law (Bertsch et al. 2000; Reinert & Bertsch 2001). The two spectral indices of 1.23 \pm 0.15 and 3.39 \pm 0.36 bracket the 3EG index of 1.86 ± 0.10 . The integral photon flux of $35 \times 10^8 \text{ cm}^{-2} \text{ s}^{-1}$ thus obtained is a bit more than half of the 3EG value, presumably because of how neighboring sources were handled. AGILE data confirm a spectral break near 2 GeV (Halpern et al. 2008).

The different approaches used in analyses of LAT data to find the background contribution and to take into account the direction- and energy-dependent instrument response are outlined in our recent analysis of LAT data for Vela (Abdo et al. 2009). One method estimates the background and pulsar spectrum by maximizing the joint likelihood for the on-pulse data, phases $0.73 < \phi < 1.05$, and the pulsed data (‘bn-o’). Another models observed neighboring sources and the diffuse Galactic, extragalactic, and residual charged backgrounds, again in a likelihood approach (‘btlike’, provided with the Fermi science tools). The ‘unfolding’ method deconvolves the observed events from the instrument response. All three methods give consistent results.

Figure 3 shows the result of the likelihood test to the data assuming a power-law spectrum with an exponential cutoff,

$$\frac{dF}{dE} = kE^{-\alpha} e^{-(E/E_c)^b}$$

where the energy E is expressed in GeV and with $b = 1$, using only the on-pulse data ($0.05 < \phi < 0.73$). The curves are the ‘btlike’ results, whereas ‘bn-o’ gives a more faithful representation of the individual source data points, which are shown. To reduce confusion from the diffuse background and neighboring sources, we fit only photons above 200 MeV and extrapolate the result to 100 MeV. The spectral parameters are listed in Table 2, including the integral energy flux $\Phi = (4.3 \pm 0.1) \times 10^{10} \text{ erg cm}^{-2} \text{ s}^{-1}$ for $E > 100$ MeV. The Pearson χ^2 value for the fit is 1.1. Applying the likelihood ratio test against a spectral model with b left free, there is no evidence to reject the simple exponential model, a super-exponential cutoff ($b = 2$) is disfavored at the 3% level, and a pure power-law ($b = 0$) is strongly excluded at 13%.

We also measure the spectra of the two pulsar peaks individually. Applying the same background model and again in posing $b = 1$ yields the additional curves shown in Figure 3 and summarized in Table 2. P2 appears to persist to higher energies in Figure 1, and the fit results formally confirm this impression. However, in light of the systematic biases at play, the data are also consistent with no significant spectral difference between the two pulses. Bridge emission in the phase interval $0.26 < \phi < 0.54$ is apparent in Figure 1. It exceeds the backgrounds from the diffuse Galactic emission and from neighboring sources with 5% significance, with a photon flux that contributes roughly 10% of the total on-pulse flux. Finally, the on-pulse data show no excess above the background, allowing us to place an upper limit on the flux of a putative gamma-ray PWN of $< 10\%$ of the

⁵⁹ <https://wikio.nrao.edu/bin/view/ICADA/GUPPIUsersGuide>

phase-averaged emission, at the 95% confidence level.

The uncertainties in Table 2 and above are statistical. Two effects dominate the systematic biases: modeling of the diffuse emission and neighboring sources over the several degree radius dictated by the point spread function at the lower energy bound; and uncertainties in the energy-dependent effective area. The latter is calculated using the test beam-verified Monte Carlo detector simulations (Baldini et al. 2007), and verified on-orbit using gamma-ray data from the Vela pulsar. For the LAT Vela spectral measurements (Abdo et al. 2009), the differences between observed and expected on-orbit gamma-ray efficiencies led to a uncertainty on the integral energy flux of $\Delta h/h = 20\%$. Since then, the differences have been found to arise from charge in the silicon tracker deposited by cosmic rays in a time window around the gamma-ray event. Gamma-ray event reconstruction and selection efficiencies below several hundred MeV are smaller than predicted, and the fluxes reported here will increase for future analyses taking the effect into account. The potential bias in the cutoff energy is of order ~ 0.5 GeV and that of the spectral index is ~ 0.1 . The conclusion that the spectral shape for PSR J2021+ 3651 is most consistent with $b = 1$ is unaffected by these issues.

4. DISCUSSION

PSR J2021+ 3651 is among the first gamma-ray pulsars to be studied using Fermi. The gamma-ray observations, combined with X-ray images and spectra as well as with radio information such as polarization, allow stricter comparison with models than was previously possible. Improved knowledge of beam geometries will in turn aid interpretation of the number counts of radio-loud and radio-quiet gamma-ray pulsars that Fermi sees.

Emission models fall into two classes: Polar cap (PC) scenarios (Dougherty & Harding 1996), which place the emission very close to the star surface, and outer magnetosphere models. Of the latter, the outer gap (OG) picture (Romani & Yadigaroglu 1995; Cheng et al. 2000; Hirotani 2005) ascribes the double pulse to emission at the boundaries of a single magnetic pole, while the two pole caustic model (Dyks & Rudak 2003), a physical realization of which may be the model version of the slot-gap (SG) picture (Musliov & Harding 2004; Harding et al. 2008), assigns the two pulses to the trailing boundaries of separate magnetic poles.

Gamma-rays created at the polar caps interact with the intense magnetic fields near the neutron star surface, resulting in superexponential spectral cut-offs below a few GeV, while OG models predict simple exponential cut-offs. LAT confirms and refines the spectral break measured with EGRET and also seen with AGILE by Halpern et al. (2008). The observed emission beyond 10 GeV and absence of a sharp cut-off indicate outer magnetosphere processes.

From the phase separation of the peaks in the gamma-ray light curve $\Delta\phi = 0.468$, lag from radio $\tau_{\text{radio}} = 0.16$, and X-ray torus-derived viewing angle $\theta = 85^\circ$, we have bounds on the pulsar geometry that constrain the possible emission models. For the PC model $\theta = 0.5$ is natural for large α and magnetic inclination; one would expect to observe both radio pulses as well, since the observer must view the emission at a small angle

to the magnetic pole to intersect the small PC beam. Indeed, Figure 1 shows a faint radio interpulse. On the other hand both outer magnetosphere models can produce two narrow gamma-ray pulses at the observed separation for $\theta = 85^\circ$. Narrow gamma-ray pulses arise naturally in outer magnetosphere models, where the peaks are formed by caustics. For OG and SG, a magnetic inclination of $\theta = 70^\circ$ is inferred. For this, the second radio pole may be faint ("grazing") or absent.

An additional radio observation supports the view that PSR J2021+ 3651 is a nearly orthogonal rotator, that is, has a large magnetic inclination. Figure 4 shows polarization data from which we determined the rotation measure (RM) of J2021+ 3651 to be $524 \pm 4 \text{ rad m}^{-2}$, and measured the polarized pulse profile. The data are insufficient to constrain the parameters of the Rotating Vector Model (RVM, Radhakrishnan & Cooke 1969): they are compatible with $\theta = 70^\circ$ found above.

The large lag from the radio pulse is a challenge for simple versions of all models using a vacuum dipole magnetosphere. For the PC model we expect $\tau_{\text{radio}} = 0$, in strong disagreement. Both the OG and SG models predict $\tau_{\text{radio}} = 0.05 - 0.1$, for radio emission at the star surface. However, recent work (Johnston & Weisberg 2006; Karastergiou & Johnston 2007) suggests that radio emission from young, Vela-type pulsars occurs over a narrow range of altitudes below roughly 100 times the radius of the neutron star, whereas for their older brethren, it extends to lower altitudes. At high altitudes aberration shifts the radio pulse forward and widens the radio cone. If only the leading edge of the cone contributes to the narrow radio pulse, then the observed lag is easily achieved.

The emission scenarios predict different relations between the gamma-ray luminosity L_γ and the spin-down power \dot{E} , making the efficiency $\eta = L_\gamma/\dot{E}$ an additional discriminating observable, especially if applied to a large sample of gamma-ray pulsars. To obtain L_γ , the pulsar's distance D must be known, and the observed integral gamma-ray energy flux \dot{h} must be extrapolated to the full sky, that is, some model of the beam shapes must be applied. In the past, the lack of geometric constraints for the small number of known gamma-ray pulsars led to the convention of simply assuming the gamma-ray beam swept out a 1 sr solid angle, from which $L_\gamma = \dot{h} D^2$; such a narrow beam is appropriate to near-surface polar cap emission. To better exploit the available data we define, following Watters et al. (2008), a correction factor f along the Earth line-of-sight θ_E as

$$f(\theta; \theta_E) = \frac{\int_0^R F(\theta; \theta_E) \sin(\theta) d\theta}{2 \int_0^{\pi/2} F(\theta; \theta_E) d\theta} \quad (1)$$

such that

$$L_\gamma = 4 \pi f \dot{h} D^2 \quad (2)$$

$F(\theta; \theta_E)$ is the gamma-ray energy flux as a function of θ and the pulsar rotation phase. In the ratio f , the numerator is the total emission over the full sky, and the denominator is the phase-averaged flux for the light curve seen from Earth. A 1 sr sky coverage corresponds to $f = \frac{1}{4} = 0.08$ and isotropic emission gives $f = 1$. Note that $f > 1$ is possible for beams that are narrow in θ , extended in ϕ , and/or have average intensity exceeding

the value sampled at E .

Polar cap models tend to have $f \approx 0.1$, while for the fan beams of outer magnetosphere models f is much larger. For the OG model we estimate $f \approx 1.05$ while the SG model has $f \approx 1.1$ for the observed (Watters et al. 2008).

The distance to PSR J2021+3651 is intriguing. The NE2001 electron density model assigns a distance of $12_{-2.7}^{+1}$ kpc to the large DM of the pulsar, but also greatly underestimates the measured scattering timescale, casting doubt on this inferred distance. Van Etten et al. (2008) place the pulsar at $D = 2$ to 4 kpc, based on the PWN properties and the neutron star thermal emission. The large positive RM presented here is consistent with a distance at or beyond 4 kpc: of the 9 pulsars within

10° of this line-of-sight with measured RMs in the ATNF database⁶⁰ (Manchester et al. 2005), those with $D < 5$ kpc have negative RMs, while four others with $D \approx 6$ to 8 kpc have positive $RM < 150$ rad m^{-2} and DM from 130 to 240 $pc\ cm^{-3}$.

For a neutron star moment of inertia of 10^{45} $g\ cm^2$ we obtain

$$\dot{E} = L = E \dot{\nu} = 0.25 f (D = 4\ kpc)^2: \quad (3)$$

High-altitude models are preferred by the pulse and spectral shapes. A 25% efficiency is amongst the largest for all known gamma-ray pulsars, taking the f values as in Table 1 of Watters et al. (2008). The nominal DM distance in poses small f , i.e., polar cap emission, whereas the smaller distances imposed by the high-altitude models leave unexplained the large observed electron column density along the line of sight to the Dragon nebula.

The open cluster Berkeley 87 is 0.5° from PSR J2021+3651. Prior to the pulsed gamma-ray detections, it was suspected to be a proton accelerator that could explain 3EG J2021+3716 and/or 3EG J2016+3657, and was searched for TeV emission (see e.g. Aharonian et al. 2006). The LAT localization clearly refutes Berkeley 87 as the dominant gamma-ray emitter in this direction, even if the α -pulse emission upper limit is near the intensity predicted by Bednarek (2007), leaving the door open for future explorations. The detailed maps in Schneider et al. (2007) include the position of PSR J2021+3651 and their re-examination may allow part of the large free electron column density to be accounted for.

5. CONCLUSIONS

PSR J2021+3651 was detected in gamma-rays in LAT data taken during Fermi instrument commissioning, with more data accumulated during the first few months of the all-sky survey. The extensive radio pulsar timing being performed for the Fermi mission facilitated the detection and enhanced the quality of the resulting light curves as well as their interpretation. A long with the dis-

covery of a pulsed signal in the gamma-ray source CTA 1 identifying a previously mysterious source (Abdo et al. 2008), this is a good example of the remarkable capability of the LAT to identify Galactic sources. Of the 171 unidentified sources in the 3rd EGRET catalog, some 30 are Galactic ($b_j < 3^\circ$) and have steady fluxes as measured by EGRET. The identification of 3EG J2021+3716 suggests that many of these other sources could also be pulsars.

The high-resolution gamma-ray light curve, the faint radio interpulse, and the polarization data, together with earlier X-ray images of the torus and jet of the surrounding pulsar wind nebula, allow comparisons with different pulsar models. The rotation measure adds an argument in favor of an intermediate pulsar distance. Re-analysis of Chandra X-ray data yields an improved light curve. Phase-resolved spectral measurements show that both peaks cut off exponentially near 2 GeV. Gamma-ray emission from the polar cap is the least plausible explanation at present, even if the outer magnetosphere models imply large gamma-ray efficiencies if PSR J2021+3651 is indeed more distant than a few kpc.

The Fermi/LAT Collaboration acknowledges generous ongoing support from a number of agencies and institutes that have supported both the development and the operation of the LAT as well as scientific data analysis. These include the National Aeronautics and Space Administration and the Department of Energy in the United States, the Commissariat à l'Énergie Atomique and the Centre National de la Recherche Scientifique / Institut National de Physique Nucléaire et de Physique des Particules in France, the Agenzia Spaziale Italiana and the Istituto Nazionale di Fisica Nucleare in Italy, the Ministry of Education, Culture, Sports, Science and Technology (MEXT), High Energy Accelerator Research Organization (KEK) and Japan Aerospace Exploration Agency (JAXA) in Japan, and the K.A.W. Allenberg Foundation, the Swedish Research Council and the Swedish National Space Board in Sweden.

Additional support for science analysis during the operations phase from the following agencies is also gratefully acknowledged: the Istituto Nazionale di Astrofisica in Italy and the K.A.W. Allenberg Foundation in Sweden for providing a grant in support of a Royal Swedish Academy of Sciences Research fellowship for JC.

The Green Bank Telescope is operated by the National Radio Astronomy Observatory, a facility of the National Science Foundation operated under cooperative agreement by Associated Universities, Inc. The Arecibo Observatory is part of the National Astronomy and Ionosphere Center (NAIC), a national research center operated by Cornell University under a cooperative agreement with the National Science Foundation.

⁶⁰ <http://www.atnf.csiro.au/research/pulsar/psrcat/>

REFERENCES

- Abdo, A. A., et al. 2008, *Science*, 322, 1218
 Abdo, A. A., et al. 2009, *ApJ*, 696, 1084
 Aharonian, F. A., et al. 2006, *A & A*, 454, 775
 Atwood, W. B., et al. 2009, *ApJS*, 697, arXiv:0902.1089
 Baldini, L., et al. 2007, *Proc. 1st GLAST Symposium*, ed. S. Ritz, P. Michelson, & C. A. Meegan, *AIP*, 921, 190
 Bednarek, W. 2007, *MNRAS*, 382, 367

TABLE 1
Radio ephemeris of PSR J2021+ 3651

Pulsar name	J2021+ 3651
Right ascension (J2000) ^a	20:21:05.46
Declination (J2000) ^a	36:51:04.8
Pulse frequency (s ⁻¹)	9.6393948581 (3)
Frequency derivative (s ⁻²)	8.89419(6) 10 ⁻¹²
Frequency 2nd derivative (s ⁻³)	1.09(5) 10 ⁻²¹
Epoch of t (MJD [TDB])	54710.0
Epoch of zero phase reference (MJD [TDB]) ^b	54715.22791423678
Range of t (MJD)	54634.18{54785.9
Dispersion measure (pc cm ⁻³) ^c	367.5 1

Note. | The digits in parentheses are the nominal TEMPO uncertainties.

^a Celestial coordinates are from Chandra observations (Hessels et al. 2004).

^b This is TEMPO's "TZRM JD" extrapolated to the solar system barycenter at infinite frequency.

^c See x2 for details of this measurement.

TABLE 2
Spectral results for PSR J2021+ 3651

Phase interval	F ^a		h ^b		E _c ^c	
	(10 ⁸ cm ² s ⁻¹)		(10 ¹⁰ ergs cm ² s ⁻¹)		(eV)	
P1	0:13 to 0:20	18 1	1:3 0:1	1:5 0:1	1:9 0:3	
P2	0:58 to 0:68	21 1	1:7 0:1	1:5 0:1	2:8 0:5	
Bridge	0:26 to 0:54	10% of Total pulse				
Total pulse	0:05 to 0:73	56 3	4:3 0:1	1:5 0:1	2:4 0:3	
Off pulse	0:73 to 1:05	< 10% of Total pulse				

^a Integral photon flux (> 100 MeV).

^b Integral energy flux (> 100 MeV). Flux systematic biases could lead to 20% increases, see text.

^c Energy of an exponential cut-off to a power-law spectrum with index .

Bertsch, D. L., Hartman, R. C., Hunter, S. D., Thompson, D. J., Lin, Y. C., Knien, D. A., Kanbach, G., Mayer-Hasselwander, H. A., Reinert, O., & Sreekumar, P. 2000, Proc. 5th Compact Symposium, ed. M. L. McConnell & J. M. Ryan, AIP, 510, 504

Bignami, G. F., & Caraveo, P. A. 1996, ARA & A, 34, 331

Cheng, K. S., Ruderman, M. A., & Zhang, L. 2000, ApJ, 537, 964

Cordes, J. M., & Lazio, T. J. W. 2002, preprint (astro-ph/0207156)

Crawford, F., Roberts, M. S. E., Hessels, J. W. T., Ransom, S. M., Livingstone, M., Tam, C. R., & Kaspi, V. M. 2006, ApJ, 652, 1499

Daugherty, J. K. & Harding, A. K. 1996, ApJ, 458, 278

Dowd, A., Sisk, W., & Hagen, J. 2000 ASPC, 202, 275

Dyks, J., & Rudak, B. 2003, ApJ, 598, 1201

Fierro, J. M., Michelson, P. F., Nolan, P. L., & Thompson, D. J. 1998, ApJ, 494, 734

Halpern, J. P., Camilo, F., Giuliani, A., Gotthelf, E. V., McLaughlin, M. A., Mukherjee, R., Pellizzoni, A., Ransom, S. M., Roberts, M. S. E., & Tavani, M. 2008, ApJ, 688, 33

Harding, A. K., Stem, J. V., Dyks, J., & Frackowiak, M. 2008, ApJ, 680, 1378

Hartman, R. C., et al. 1999, ApJS, 123, 79

Hessels, J. W. T., Roberts, M. S. E., Ransom, S. M., Kaspi, V. M., Romani, R. W., Ng, C.-Y., Freire, P. C. C., & Gaensler, B. M. 2004, ApJ, 612, 389

Hirokani, K. 2005, Ap&SS, 297, 81

Hobbs, G., Lyne, A. G., Kramer, M., Martin, C. E., & Jordan, C. 2004, MNRAS, 353, 1311

Hotan, A. W., van Straten, W., & Manchester, R. N., 2004, PASA, 21, 302

Johnston, S., & Weisberg, J. M. 2006, MNRAS, 368, 1856

Kaplan, D. L., Escoffier, R. P., Lacasse, R. J., O'Neil, K., Ford, J. M., Ransom, S. M., Anderson, S. B., Cordes, J. M., Lazio, T. J. W., & Kulkarni, S. R. 2005, PASP, 117, 643

Karastergiou, A., & Johnston, S. 2007, MNRAS, 380, 1678

Kaspi, V. M., Roberts, M. S. E., & Harding, A. K. 2006, in Compact Stellar X-ray Sources, ed. W. Lewin & M. van der Klis (Cambridge: CUP), 279

Kramer, M., et al. 2003, MNRAS, 342, 1299

Lamb, R. C., & Maccomb, D. J. 1997, ApJ, 488, 872

Manchester, R. N., Hobbs, G. B., Teoh, A., & Hobbs, M. 2005, AJ, 129, 1993

McLaughlin, M. A., & Cordes, J. M. 2004, in X-ray and Gamma-ray Astrophysics of Galactic Sources, ed. M. Tavani, A. Pellizzoni, & S. Vercellone (Rome: IASF), 67

Muslimov, A. G., & Harding, A. K. 2004, ApJ, 606, 1143

Radhakrishnan, V., & Cooke, D. J. 1969, Astrophys. Lett., 3, 225

Reinert, O., & Bertsch, D. L. 2001, International Cosmic Ray Conference, ICRC, 6, 2546

Roberts, M. S. E., Romani, R. W., & Kawai, N. 2001 ApJS, 133, 451

Roberts, M. S. E., Hessels, J. W. T., Ransom, S. M., Kaspi, V. M., Freire, P. C. C., Crawford, F., & Lorimer, D. R. 2002, ApJ, 577, L19

Romani, R. W., & Yadigaroglu, I. A. 1995, ApJ, 438, 314

Schneider, N., et al. 2007, A & A, 474, 873

Smith, D. A., et al. 2008, A & A, 492, 923

Standish, E. M., JPL Planetary and Lunar Ephemerides, DE405/LE405, Memo IOM 312.F-98-048 (1998)

Thompson, D. J. 2004, in Cosmic Gamma-ray Sources, ed. K. S. Cheng & G. E. Romero (Dordrecht: Kluwer), 149

Van Etten, A., Romani, R. W., & Ng, C.-Y. 2008, ApJ, 680, 1417

Watters, K. P., et al. 2009, ApJ, 695, 1289

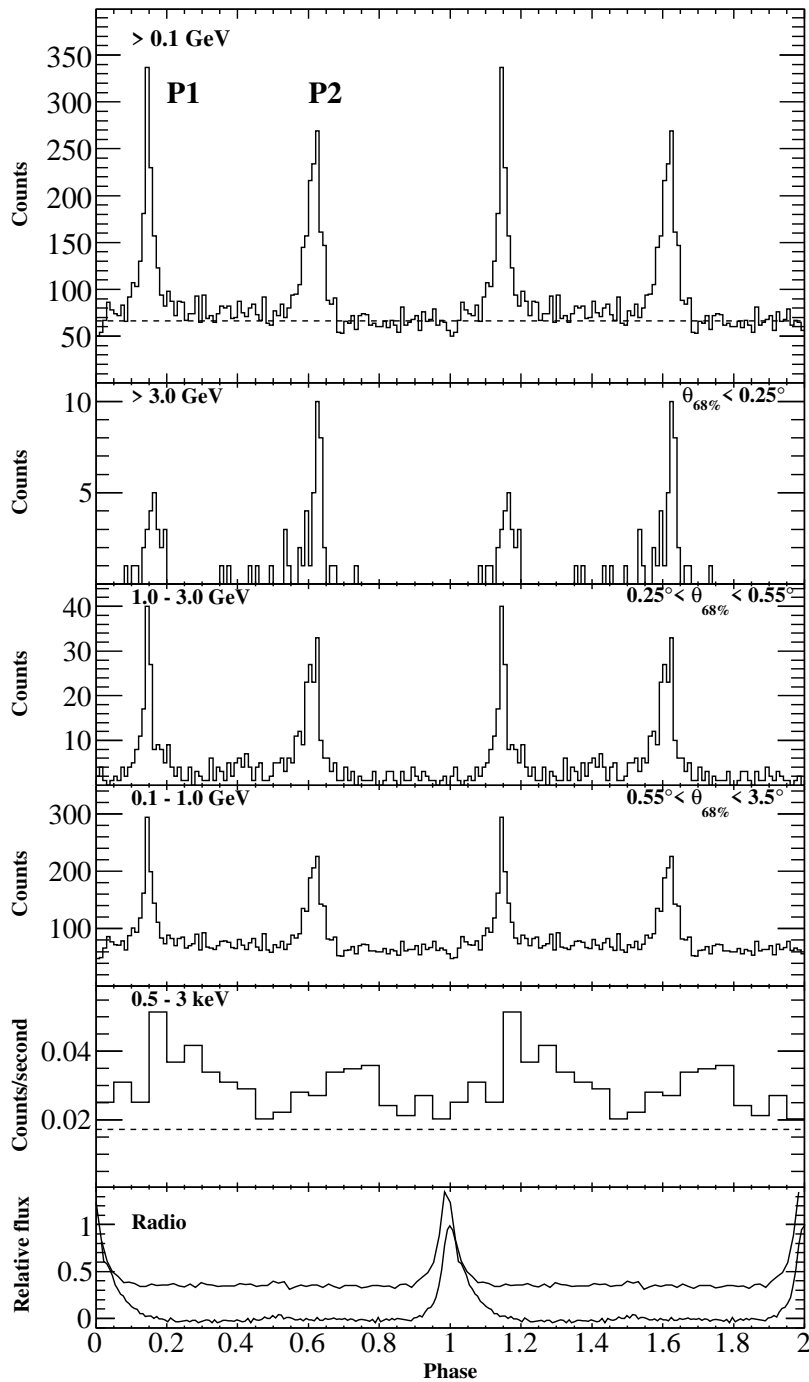


Fig. 1. Top frame: Light curve for PSR J2021+3651, for γ -rays with energy > 100 MeV within the energy-dependent 68% containment radius $\theta_{68\%}$ of the pulsar position. Each bin is 0.01 in phase, and 2 rotation cycles are shown. The horizontal dashed line shows the average number of counts in the δ -pulse phase interval. Three following frames: Light curves in the three indicated energy ranges. Second frame from bottom: Phase-aligned Chandra ACIS-S CC X-ray light curve, with the background rate shown by the horizontal dashed line. Bottom frame: The upper curve is the 1950 MHz radio profile obtained using the Pulsar Spigot at the Green Bank Telescope. The lower curve is the total intensity profile obtained at Arecibo using the WAPP spectrometers with a 3.7 hr integration time and 300 MHz of bandwidth centered at 1500 MHz, vertically offset from the GBT curve for clarity. Both curves show evidence for an interpulse at phase 0.5 with amplitude $\sim 5\%$ of the main pulse.

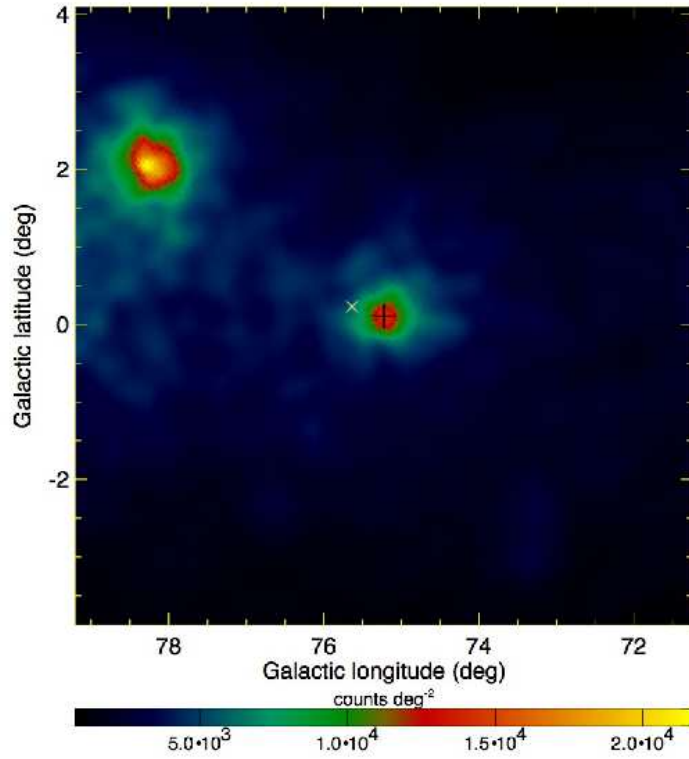


Fig. 2. | G am m a-ray counts per square degree, w ith $E > 100$ M eV, centered at the Chandra-derived position of P SR J2021+ 3651. B in sizes vary such that statistical u ctuations are x ed to a signal-to-noise ratio of 10. The cross indicates the Chandra-derived position of P SR J2021+ 3651. The \ "X" indicates the position of the open cluster Berkeley 87. The bright ob ject at upper-left is 3EG J2020+ 4017.

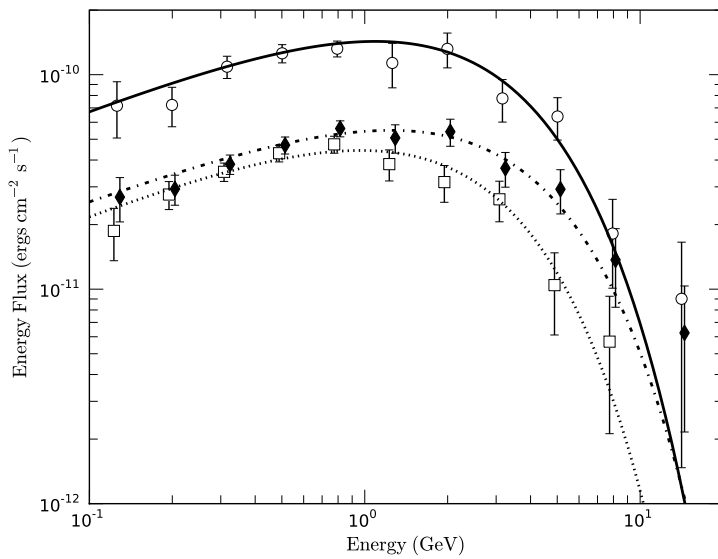


Fig. 3. | Spectral energy distribution $E^2 dF = dE$ for P SR J2021+ 3651 as t by \gtlike" assum ing a power-law spectrum w ith an exponential cuto , for P1 (dotted), P2 (dot-dash), and Total pulse (solid). The differential values as estimated by \on o " are given for P1 (squares), P2 (diamonds), and Total pulse (circles). The error bars are statistical only. For clarity, the points for P1 (P2) are plotted 25% lower (higher) in energy than for Total pulse.

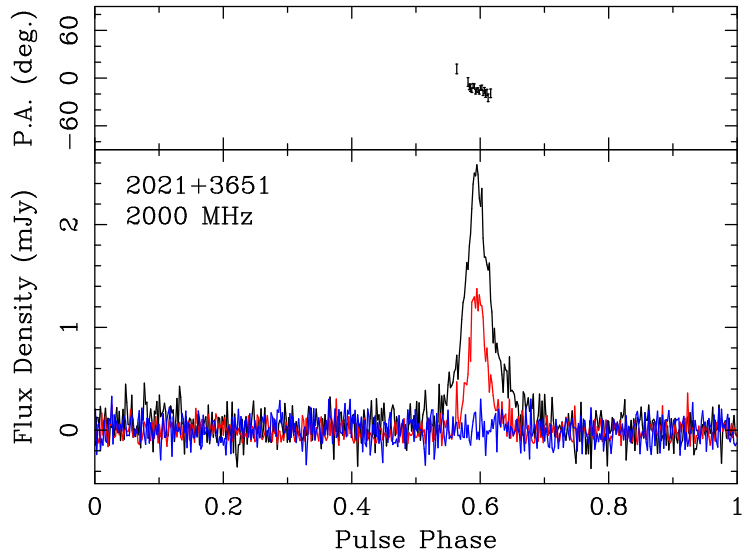


Fig. 4. | Bottom : Polarization- and flux-calibrated profile for PSR J2021+3651 obtained with the GUPPI spectrometer at the GBT. The black trace corresponds to total intensity, the red to linear polarization, and the blue to circular polarization (greatest to least intensity at 0:6, respectively). The phase reference is different from Fig. 1. The faint interpulse is visible near phase 0:1. Top: Position angle of linear polarization, corrected to the pulsar frame, accounting for the Faraday rotation implied by the large rotation measure of $RM = 524 \pm 4 \text{ rad m}^{-2}$.